Dimethylammonium gallium sulfate hexahydrate and dimethylammonium aluminium sulfate hexahydrate—members of a crystal family with exceptional commensurate/incommensurate phase sequences

2005 J. Phys.: Condens. Matter 17 4511

(http://iopscience.iop.org/0953-8984/17/28/010)

INSTITUTE OF PHYSICS PUBLISHING JOURNAL OF PHYSICS: CONDENSED MATTER

J. Phys.: Condens. Matter **17** (2005) 4511–4529 doi:10.1088/0953-8984/17/28/010

Dimethylammonium gallium sulfate hexahydrate and dimethylammonium aluminium sulfate hexahydrate—members of a crystal family with exceptional commensurate/incommensurate phase sequences

G Völkel[1], R Böttcher[1], D Michel[1], Z Czapla[2] and J Banys[3]

[1] Universität Leipzig, Fakultät für Physik und Geowissenschaften, Linnéstrasse 5, D-04103 Leipzig, Germany
[2] Institute of Experimental Physics, University of Wroclaw, Maxa Borna 9, PL-50204 Wroclaw, Poland
[3] Faculty of Physics, Vilnius University, Sauletekio 9, 2040 Vilnius, Lithuania

Received 22 March 2005, in final form 13 June 2005
Published 1 July 2005
Online at stacks.iop.org/JPhysCM/17/4511

Abstract

Dimethylammonium gallium sulfate hexahydrate (DMAGaS) and dimethylammonium aluminium sulfate hexahydrate (DMAAS) are isomorphous and ferroelastic at room temperature. But at lower temperatures their ordering behaviours are quite different. Whereas DMAAS shows only a single order–disorder-type transition into a ferroelectric phase, DMAGaS exhibits an exceptional sequence of commensurate and incommensurate phases with an antiferroelectric lock-in phase at low temperatures. The basic experimental findings from recent pressure and composition dependent dielectric investigations and from electron paramagnetic resonance studies are briefly reviewed. Experimental results are then discussed within the framework of the semimicroscopical extended discrete frustrated φ^4 (DIFFOUR) model. The frustrating nearest and next nearest neighbour interactions between the dimethylammonium (DMA) dipoles in the $-DMA_{(i)}-Ga/Al(H_2O)_{6(i)}-DMA_{(i+1)}-Ga/Al(H_2O)_{6(i+1)}-$ chains give rise to the observed complex phase sequence. It will be shown that the phase sequence of DMAGaS, its variation under pressure and with DMAAS admixture, as well as the new pressure induced phases of DMAAS can be well interpreted by theory.

1. Introduction

For more than twenty years intensive research has been done on the ferroelectric crystals dimethylammonium gallium sulfate hexahydrate (DMAGaS), $(CH_3)_2NH_2Ga(SO_4)_2{\cdot}6H_2O$, and the isomorphous dimethylammonium aluminium sulfate hexahydrate (DMAAS),

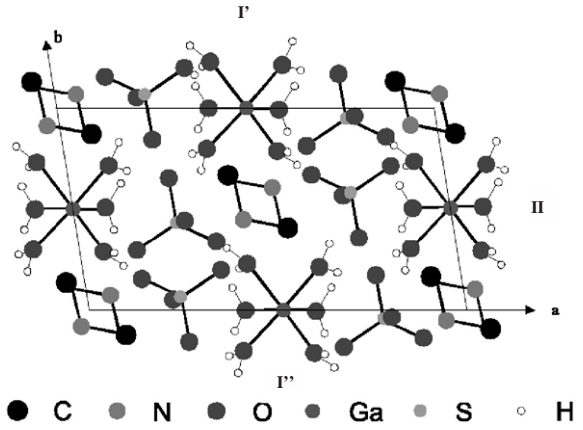

Figure 1. Crystal structure of DMAGaS at room temperature. The unit cell is projected on the (001) plane of the **abc** system (after [13]). The hydrogen atoms of the dimethylammonium ions as well as the two additional nitrogen positions along and opposite to the **c** axis are left out.

$(CH_3)_2NH_2Al(SO_4)_2{\cdot}6H_2O$ [1–9]. In the last decade among the main questions of interest were the reason for the diversity in their low temperature behaviours and the nature of the rather strange non-polar low temperature phase of DMAGaS. But nobody suspected that DMAGaS could belong to the interesting family of incommensurate ferroelectrics and that (although much less surprising) it could be the only IC ferroelectric with an antiferroelectric ground state phase. This new insight came only very recently from electron paramagnetic resonance (EPR) studies done on ($\lessapprox$0.03 wt%) chromium doped DMAGaS [10]. In the same paper it was also concluded that the extended discrete frustrated φ^4 (DIFFOUR) model [11] should be qualified to give a correct description of this new unusual phase sequence.

DMAGaS and DMAAS belong to a crystal family with the further members dimethylammonium aluminium sulfate selenate hexahydrate, $(CH_3)_2NH_2Al(S_{1-x}Se_xO_4)_2{\cdot}6H_2O$, and the solid solutions dimethylammonium gallium aluminium sulfate hexahydrate, $(CH_3)_2NH_2Ga_{1-x}Al_x(SO_4)_2{\cdot}6H_2O$. The crystal structure is built up of Ga or Al cations coordinating six water molecules, regular SO_4 or SeO_4 tetrahedra and $[(CH_3)_2NH_2]^+$ (DMA) cations where all these units are interconnected by a three-dimensional framework of hydrogen bonds (figure 1). In their high temperature phases, ferroelastic DMAGaS and DMAAS crystals were found to be isomorphic in structure and to belong to the monoclinic space group $P2_1/n$. Both crystals exhibit a structural transition into a ferroelectric phase. The ferroelectric transition is regarded to be of order–disorder type. The process of ordering of the dimethylammonium cations and not that of the protons in the hydrogen bond system is the driving force for the ferroelectric transition [12, 13]. DMAAS undergoes only one transition of second order at $T_C = 152$ K into a ferroelectric phase. This phase is stable until the lowest temperatures are reached. The ferroelectric transition is associated with the polar dimethylammonium cations which execute hindered rotations around their C–C direction in the ferroelastic phase and then order statistically in the ferroelectric phase along the polar direction. At the transition into the ferroelectric phase the twofold screw axis disappears and the crystal adopts a structure with the space group Pn. A spontaneous polarization results along the glide direction of the glide mirror plane n. For a long time it was only known that in contrast DMAGaS shows two successive first-order transitions, a first one into a ferroelectric phase at $T_{C1} = 134$ K and a second one into a low temperature non-polar phase at $T_{C2} = 115$ K. The reason for this difference in

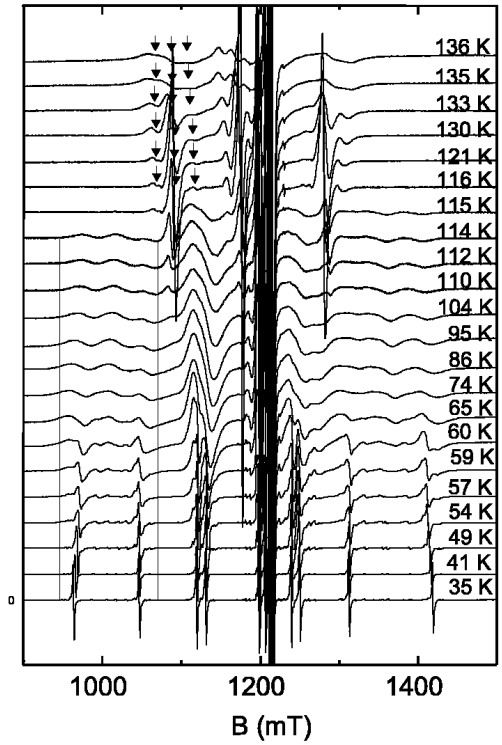

Figure 2. Temperature dependence of the Q band Cr^{3+} EPR spectra of DMAGaS for a selected magnetic field direction within the **bc** plane forming an angle of 25° to the **b** direction. The above-mentioned triplets related to the paraelectric and ferroelectric phases and positioned at about 1100 mT are marked by arrows. In the low temperature phases, the low field EPR transitions are labelled by the two parallel lines [10].

behaviour of DMAAS and DMAGaS was not understood. Both the ferroelectric transitions of DMAAS and DMAGaS are close to a tricritical behaviour whereas the transition into the non-polar phase in DMAGaS is strongly of first order. A simple Landau description as well as a microscopic four-state Hubbard model were proposed to describe these phenomena [14, 15].

In recent years, measurements of the ^{71}Ga, ^{27}Al and ^{1}H NMR in DMAGaS and DMAAS [12, 16] as well as the Cu^{2+} and Cr^{3+} EPR [17, 18] in DMAAS have been performed in order to study the microscopic nature of the ferroelectric transition. Recent Q band EPR measurements at 34.4 GHz on paramagnetic Cr^{3+} ions substituting at Al^{3+} sites in chromium doped DMAAS [13, 19] showed that the occupation probabilities w^+ and w^- of the two polar configurations of the dimethylammonium cations exhibit a temperature dependence in agreement with the macroscopic spontaneous polarization. This is experimental proof of the driving role of the dimethylammonium cations at the ferroelectric transition. However, the dimethylammonium order is not of static but of dynamic nature. The rotational motion of the individual dimethylammonium groups never freezes out and remains throughout faster than the extremely slow critical dielectric relaxation.

In recent papers [10, 20–22] we reported on EPR measurements on chromium doped DMAGaS performed in the Q band at 34 GHz in the temperature range from room temperature down to liquid helium temperature. In the ferroelastic and ferroelectric phases measurements show the Cr^{3+} EPR spectra to be very similar to those of DMAAS. Passing the transition into

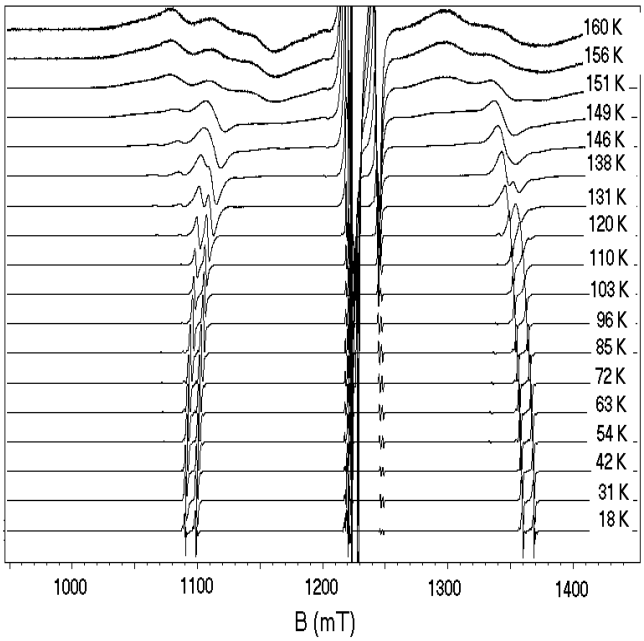

Figure 3. Temperature dependence of the Cr^{3+} EPR spectra of a chromium doped DMAAS single crystal at Q band. The magnetic field direction is very close to the crystallographic **c** direction [21] such that the spectra of the Cr^{3+} ions at sites I and II appear well resolved below 138 K. In contrast to the DMAGaS case, the spectra show clearly that the ferroelectric phase is stable down to the lowest temperatures.

the non-polar phase at $T_{C2} = 115$ K, striking changes have been observed in the DMAGaS spectra in the form of large line shifts, line broadening and in particular a multiplied number of lines. However, at a temperature of about 60 K the spectra show a conspicuous simplification—ending up with very sharp lines in the low temperature region where the number of lines is doubled in comparison to the ferroelastic phase case. The latter indicates a unit cell doubling in the low temperature phase at least below 60 K whereas above this temperature the spectra refer to intermediate phases with a tremendous disorder in the dimethylammonium cation system. A thorough spectrum interpretation and modelling of the phase sequences of DMAGaS were done [10]. The line shape shows no edge singularity as usually observed in magnetic resonance experiments for incommensurately modulated crystals [23]. The reason is that the DMA order parameter is associated with changes of the line intensities only and not with shifts of line positions. The redeveloped line shape simulations admitted the conclusion that below $T_{C2} = 115$ K a whole sequence of modulated phases does exist with varying modulation periods ending with a transition into an antiferroelectric phase below 60 K. The phase diagram of DMAGaS appears as complicated as that of the well known model system betaine calcium chloride dihydrate (BCCD). The phase sequence in DMAGaS, with a paraelectric–ferroelectric transition at high temperatures, incommensurate and commensurate phases at medium temperatures and an antiferroelectric phase at low temperatures, is quite unique and to our knowledge not yet been observed in any other crystal. We explained this unusual sequence of phases by means of a Landau approach using a greater number of sublattice polarizations. Furthermore, we showed the Landau potential used is very similar but not identical to the more general DIFFOUR potential [11].

On the other hand, very interesting and fundamental experiments have been reported dealing with the influence of high hydrostatic pressure on the phase diagrams of DMAAS and DMAGaS [9, 8]. It was shown that under high hydrostatic pressure the ferroelectric phase of DMAGaS disappears whereas in DMAAS new phases of unknown character appear between paraelectric and ferroelectric phases. Last but not least, it was shown very recently that an admixture of 10% DMAAS into a DMAGaS crystal leads to a remarkable decrease of the transition temperature from the ferroelectric to the modulated phase but to almost no change of the paraelectric–ferroelectric transition temperature T_{C1} [25].

The aim of the present paper is to present a uniform model description of the most important and until now unexplained ordering phenomena observed in these crystals within the framework of the extended DIFFOUR model. Along the way, it is inevitable that we will refer to some of the most important experimental facts published recently for comparison with the model calculations. The composition dependence of the transition temperatures is, like the pressure dependence, an important touchstone for theory. We present a new experimental confirmation of the antiferroelectric character of the low temperature phase of DMAGaS using a high resolution EPR five-pulse technique. This investigation is unique as regards the technique applied and confirms definitely that two structurally identical Cr_{Ga} sites in neighbouring unit cells in the ferroelectric and paraelectric phases become structurally unequal in the low temperature phase. With the approach of pressure and composition dependent model parameters, we will show that the extended DIFFOUR model is a convincing theoretical concept for modelling the experimental observations.

The paper is organized as follows. Section 2 refers briefly to the experimental results reported in the literature as well as to those obtained from recent measurements. Section 3 gives a short account of key aspects of the extended DIFFOUR model and resulting phase diagrams. In section 4 the experimental findings are qualitatively discussed with respect to the extended DIFFOUR model and conclusions are drawn in the last section.

2. Summary of experimental findings

2.1. EPR results

2.1.1. cw-EPR measurements at Q band. In the paraelectric and ferroelectric phases, the Cr^{3+} EPR spectra of DMAAS and DMAGaS are very similar [10, 13]. The rotation patterns show two magnetically equivalent sets of triplets in accordance with the two chemically equivalent Al or Ga sites in the unit cell which are statistically replaced to less than tenth of a per cent by Cr^{3+} ions. The spin Hamiltonian $\mathbf{H} = \beta\mathbf{BgS} + \mathbf{SDS}$ describes the spectra, where $\mathbf{S}$ is the electron spin operator of the Cr^{3+} ion, β is the Bohr magneton, $\mathbf{g}$ is the g tensor and $\mathbf{D}$ the is fine structure tensor. In selected directions, the temperature dependences of the Q band EPR spectra were measured from room temperature down to liquid helium temperature (figures 2 and 3). On cooling, a very heavy line broadening appears in the paraelectric phase and a line tripling of the fine structure split lines already occurs far above T_{C1}. Passing the ferroelectric transition, the intensity ratio of the triplet satellite to the centre triplet line decreases. In DMAAS on further temperature reduction, the spectra change only smoothly without any jump or other splitting (figure 3). This shows that no further phase transition occurs. In contrast, at the transition temperature $T_{C2} = 115$ K of DMAGaS, the spectrum changes abruptly (figure 2). Large shifts of line positions, striking line broadening and multiplication of the number of lines appear showing a considerable thermal hysteresis. Below $T_{C3} = 55$ K the spectra simplify and narrow considerably. However, in this phase the number of persisting lines is doubled in comparison to those for the paraelectric and ferroelectric phases. This is a clear indication of a doubling of the unit cell along b, the direction of the –DMA–$Ga(H_2O)_6$–DMA– chains.

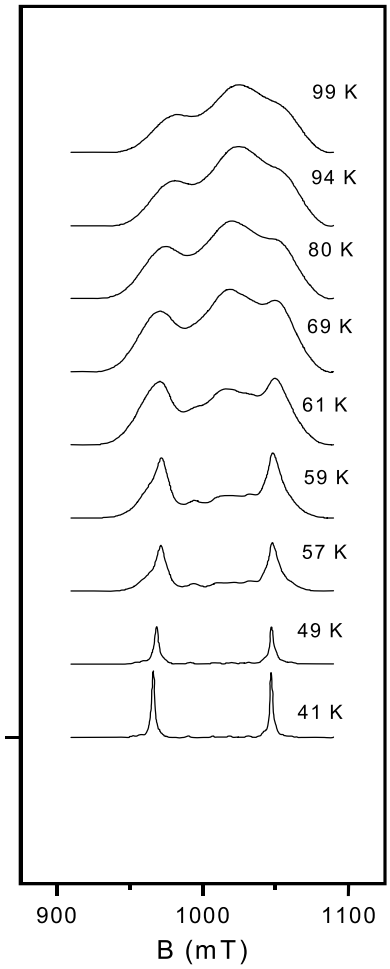

Figure 4. Temperature dependence of the integrated Cr^{3+} EPR spectra of DMAGaS shown in figure 2 in the range between 900 and 1100 mT [10].

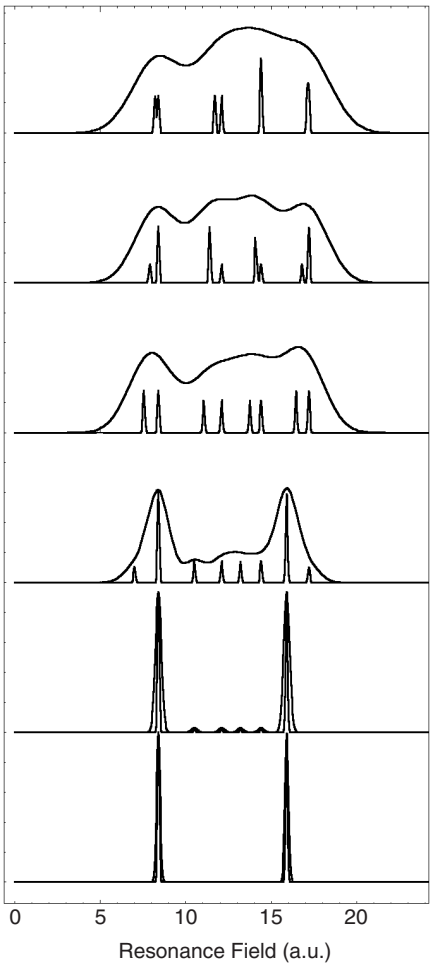

Figure 5. Simulation of the spectra presented in figure 4. The line positions of the simulated spectrum at the bottom were adopted for the experimental low temperature spectrum; slight changes were introduced for the others, as mentioned in the text. The parameters are taken to be $p(T - T_m) = \{0.95, 0.92, 0.88, 0.85, 0.80, 0.70\}$, $\Delta B_G = \{0.15, 0.25, 0.9, 1.65, 1.7, 2.0\}$, $q = \{\frac{1}{2}, \frac{1}{2} - 0.000\,01, \frac{1}{2} - 0.000\,03, \frac{1}{4} + 0.04, \frac{1}{4}, \frac{1}{4} - 0.005\}$ and $\varphi = \{0, 0, 0, 0, \pi/4, \pi/4\}$ for the six simulations from bottom to top. The abscissa is scaled in arbitrary units (au). The slim peaks mark the line positions [10].

The peculiar spectrum shape (figure 4) in the temperature range between T_{C2} and T_{C3} can be qualitatively simulated in terms of a modulation of the DMA order parameter $p(x_i) = p(T - T_{C2})\cos(2\pi q x_i + \varphi)$ along the DMA–Ga(Cr)–DMA direction [10] where $p(T - T_{C2})$ is the temperature dependent order parameter amplitude, φ is the order parameter phase and q is the wavevector of the modulation. However, in our case the line shape shows no edge singularity as usually observed in magnetic resonance experiments for incommensurately modulated crystals [23] because the DMA order parameter is associated with changes of the line intensities and not with changes of line positions. The six simulations shown in figure 5 from bottom to top are

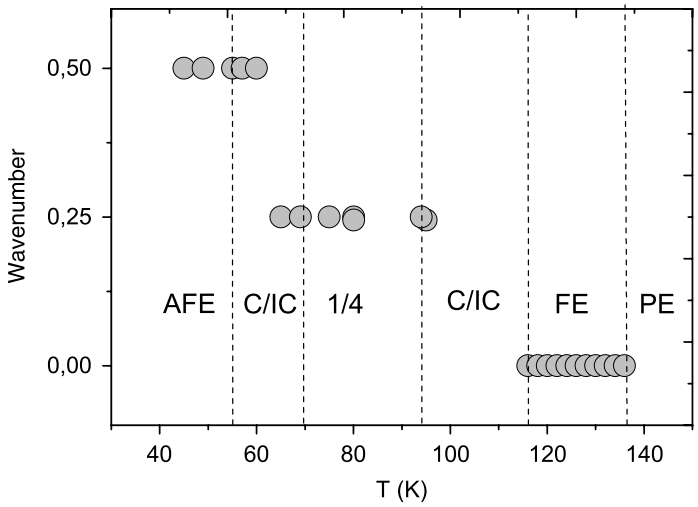

Figure 6. Temperature dependence of the wavenumbers of the modulated phases and estimated C/IC transition temperatures of chromium doped DMAGaS.

Table 1. Wavenumbers resulting from a comparison of calculated and measured EPR spectra at the various temperatures.

Temperature (K)											
45	49	55	57	60	65	69	75	80	94	95	$\geqslant$116
Wavenumber											
0.500 00	0.500 00	0.499 99	0.499 99	0.499 97	0.250 02	0.250 00	0.250 00	0.250 00	0.250 00	0.245	0

performed using order parameter amplitudes $p(T-T_{C2}) = \{0.95, 0.92, 0.89, 0.80, 0.75, 0.7\}$, wavenumbers $q = \{\frac{1}{2}, \frac{1}{2} - 0.000\,01, \frac{1}{2} - 0.000\,04, \frac{1}{4} + 0.000\,017, \frac{1}{4}, \frac{1}{4} - 0.041\,23\}$ and phases $\varphi = \{0, 0, 0, \pi/4, \pi/4, \pi/4\}$ for optimum approximation. The line positions of the two quartets used in the simulations were adopted for the well resolved low temperature spectra, only slightly changed. A Gaussian line shape has been applied with linewidth changing from 0.3 to 2.3 resonance field units as defined in figure 5. A comparison with the experimental spectra of figure 4 shows that the most characteristic spectrum changes such as the transmutation from a symmetric low temperature spectrum with two sharp lines to the asymmetric multiline spectrum at higher temperatures are very well reproduced. Successful reproductions have been achieved for other magnetic field directions too [10]. The wavenumbers evaluated, resulting from a comparison of calculated and measured EPR spectra at the various temperatures, are shown in table 1. They allow an estimate of the transition temperatures of the C/IC transitions to be obtained, as illustrated in figure 6. These results evidence that at $T_{C2} = 115$ K DMAGaS undergoes a transition from the ferroelectric phase to a sequence of modulated phases. Below 100 K there exists an IC phase with wavenumbers drawing near to $\frac{1}{4}$ at 94 K. Between 94 and 70 K a distinct commensurate $\frac{1}{4}$ phase occurs. This phase is followed by two IC phases with wavenumbers slightly above to $\frac{1}{4}$ below 70 K up to 65 K and close to $\frac{1}{2}$ from 60 to 55 K with a drastic jump of wavenumbers in between. An intermediate commensurate 1/3 phase could not be identified from the spectra. Below $T_{C3} = 55$ K, the Q band EPR spectra indicate clearly an antiferroelectric phase. The direction of modulation does not coincide with the ferroelectric direction; it is parallel to the crystalline b axis along the chains –$DMA_{(i)}$–$Ga(H_2O)_{6(i)}$–$DMA_{(i+1)}$–$Ga(H_2O)_{6(i+1)}$– of the ordering DMA dipoles.

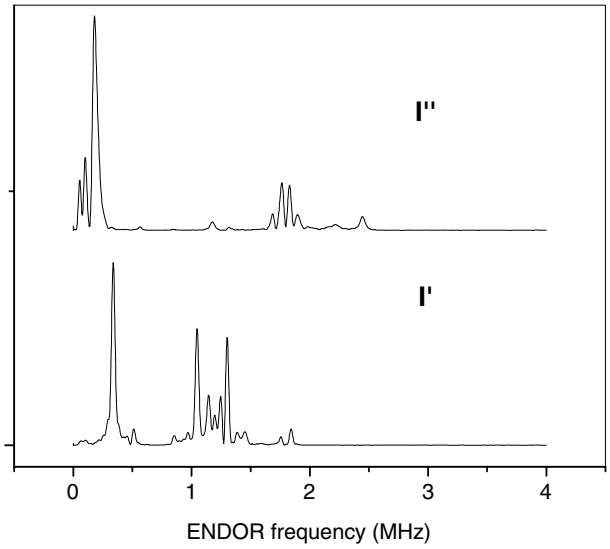

Figure 7. Five-pulse (ENDOR) spectra of the neighbouring sites I′ and I″ with the magnetic field direction 5° close to the crystallographic *c* axis in the *bc* plane.

2.1.2. EPR five-pulse measurements at X band. In order to confirm the antiferroelectric character of the low temperature phase below 60 K, high resolution EPR pulse experiments have been performed at 10 K giving sensitive structural information about the probe environment, like electron–nuclear double-resonance (ENDOR) investigations. EPR investigations done at 23 K showed that the unit cell contains not two but four magnetically distinguishable Cr probe sites which is an indication of unit cell doubling. In the paraelectric and ferroelectric phases two neighbouring Ga sites along the *b* axis are identical because they belong to identical sites in two neighbouring unit cells (see figure 1). This is no longer the case in the low temperature phase. EPR results [10] show that the two sites are twisted against each other by 15° around the *c* axis. The local order at these neighbouring Ga sites, referred to as I′, I″ and II′, II″, respectively, must mirror the antiferroelectrical order along the *b* axis. Following figure 1 or figure 2 of [10], this means that if e.g. site I′ shows the configuration with two far nitrogens, then site I″ must show that one with two close nitrogens. Consequently, the two sites I′ and I″ or similarly II′ and II″, respectively, are no longer chemically or structurally equivalent. EPR cannot be used to discriminate different chemical structures of these four sites. But the ENDOR spectra of these sites should directly reflect their structural differences because of the different ^{14}N hyperfine couplings for the two configurations. For experimental reasons it is difficult to investigate ^{14}N hyperfine couplings of the order of 1 MHz by means of stationary ENDOR techniques. Therefore, high resolution EPR pulse methods were applied. A five-pulse echo sequence $\pi_y/2$–τ–π_y–τ–$\pi_x/2$–T–$\pi_x/2$–τ–π_x–τ–echo is well suited for studying small couplings [24]. The echo decays have been Fourier transformed, resulting in ENDOR-like spectra as shown in figure 7 for site I′ and site I″, respectively, where the magnetic field direction is in the *bc* plane forming an angle of 5° with the *c* axis. The resonance fields were 4908 and 4493 G, respectively. The obviously strong differences of the ENDOR spectra cannot be explained with the field difference or with an experimental misalignment—only with different ^{14}N hyperfine couplings of the two sites, which is clear confirmation of the antiferroelectric order.

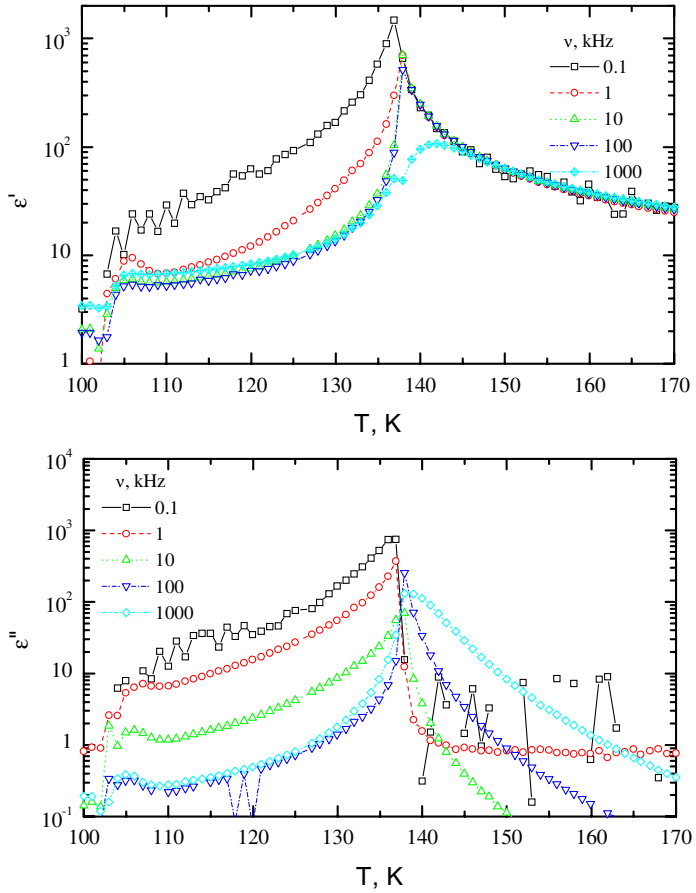

Figure 8. Temperature dependence of the real and imaginary parts of the dielectric permittivity of a $(DMAGaS)_{0.9}(DMAAS)_{0.1}$ mixed crystal.

(This figure is in colour only in the electronic version)

2.2. *Dielectric measurements*

2.2.1. The solid solution $(CH_3)_2NH_2Al_xGa_{1-x}(SO_4)_2{\cdot}6H_2O$. Dielectric measurements of the mixed crystal $(DMAGaS)_{0.9}(DMAAS)_{0.1}$ have been performed in the frequency range from 10 Hz to 1 MHz [25]. Figure 8 presents the temperature dependences of the real and imaginary parts of the dielectric permittivity for five selected frequencies, 100 Hz, 1 kHz, 10 kHz, 100 kHz and 1 MHz. A Debye-type dielectric dispersion has been observed for the soft relaxational mode in the paraelectric phase. In the intermediate ferroelectric phase two relaxational processes have been observed. The faster one is related to the soft mode and can be described with the Cole–Cole formula

$$\varepsilon^{+} = \varepsilon_{\infty} + \frac{\Delta\varepsilon}{1 + \mathrm{i}\,(\omega\tau)^{1-\alpha}} \tag{1}$$

due to a distribution of the relaxation times. At the phase transition temperature T_{C1} the soft mode softens up to 411 kHz. The activation energy of the soft mode in the paraelectric phase has been obtained as $\Delta F/k = 1248$ K (0.108 eV) which is very close to that, $\Delta F/k = 0.09$ eV, of pure DMAGaS [26]. The reciprocal value of the contribution of the soft relaxational mode

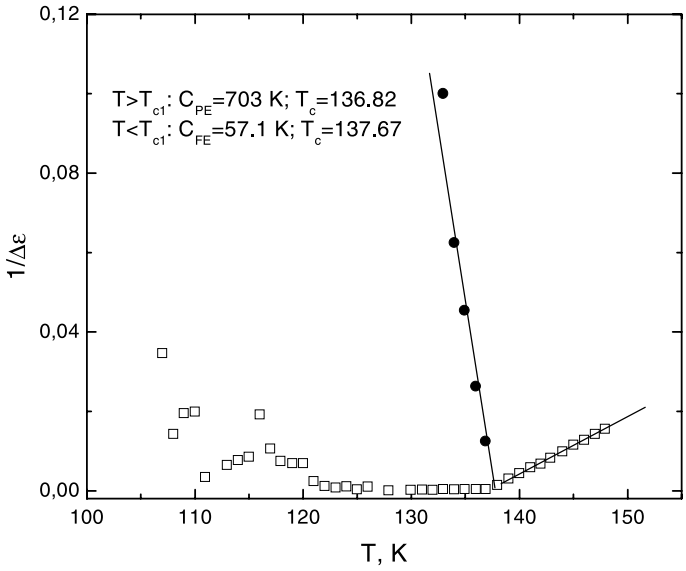

Figure 9. Temperature dependence of reciprocal contributions of the soft relaxational modes. Lines are best fits with the Curie–Weiss law.

to the dielectric permittivity, $1/\Delta\varepsilon$, shows a temperature dependence according to the Curie–Weiss law as demonstrated in figure 9. The temperature of the phase transition from the paraelectric to the ferroelectric phase has been found to be $T_{C1} = 137$ K—slightly higher than for pure DMAGaS, whereas the temperature of the transition from the ferroelectric to the non-polar phase is appreciably shifted down, to $T_{C2} = 104$ K.

With the transition to the modulated phases the critical wavevector is shifted closer to the border of the Brillouin zone. Finally, the phase transition to the antiferroelectric phase takes place when the wavevector achieves the border of the Brillouin zone. Due to that, dielectric measurements are not very well suited for the detection of such phase transitions, and at the incommensurate–antiferroelectric phase transition temperature we expect extremely small changes in the static dielectric permittivity. At low temperatures where the modulated phases have been observed using EPR, the dielectric permittivity is dominated by a low frequency dispersion perhaps caused by the water dipoles which are similar to those of a dipolar glass. This low frequency dispersion covers all the other contributions of the modulated phases and makes it difficult to recognize the step-like jump of the permittivity at the transition into the antiferroelectric phase.

2.2.2. DMAGaS under hydrostatic pressure. Dielectric measurements of the relative permittivity ϵ along the ferroelectric axis of DMAGaS were made at 1 kHz under applied hydrostatic pressure up to 35 MPa [9]. Also under pressure, in the paraelectric phase the permittivity obeys a Curie–Weiss law with only a small variation of the parameters. With rising pressure up to 8 MPa, the Curie constant changes from 3761 to 3927 K and the temperature difference $\Delta T = T_{C1} - T_0$ between the phase transition temperature T_{C1} and the Curie–Weiss temperature T_0 varies from 1.4 to 2.4 K. However, it was found that at a critical pressure of $p_t = 8.75$ MPa the dielectric permittivity changes strikingly. At lower pressure the real part of the permittivity shows a sharp peak at T_{C1} and a step-like anomaly at T_{C2} on cooling. With increasing pressure, the transition temperature T_{C1} decreases slightly at a

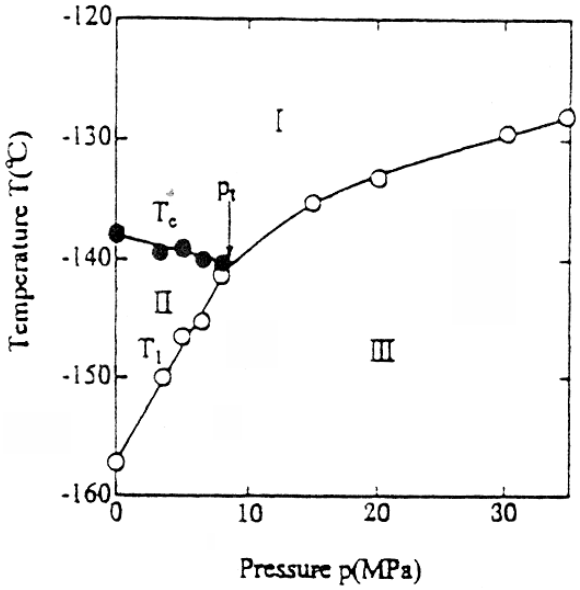

Figure 10. Pressure–temperature phase diagram of DMAGaS (from [9]).

rate $\mathrm{d}T_{C1}/\mathrm{d}p = -0.277\ \mathrm{K\ MPa^{-1}}$ whilst T_{C2} rises rapidly at a rate $\mathrm{d}T_{C1}/\mathrm{d}p = 1.95\ \mathrm{K\ MPa^{-1}}$. At the same time the peak value of ϵ at T_{C1} decreases continuously while the value of ϵ at T_{C2} increases. The result is a reduction of the temperature range where the ferroelectric phase exists. At a triple point at $p_t = 8.75$ MPa, $T_t = 132.85$ K both the transition temperatures T_{C1} and T_{C2} coincide and the ferroelectric phase disappears. P–E hysteresis loops were reported with 30 Hz alternating electric field E applied along the ferroelectric axis. Double hysteresis loops observed just above T_{C1} at atmospheric pressure as well as at 8 MPa confirm the first-order character of the paraelectric–ferroelectric transition. At the transition temperature T_{C2} the hysteresis loop vanishes abruptly. The P–E relation becomes linear with a slope as small as above T_{C1}. This was checked down to 103 K. At pressures lower than p_t, the spontaneous polarization P_S jumps up near T_{C1} with cooling and then increases gradually until it vanishes abruptly at T_{C2}. As T_{C2} increases with rising pressure the maximum value attained by the spontaneous polarization P_S is reduced. The coercive field shows behaviour that conforms, with the exception that it increases with increasing pressure. From these experimental results the pressure–temperature phase diagram has been determined as shown in figure 10, where T_C and T_1 correspond to T_{C1} and T_{C2} in our notation, respectively. The transition temperatures presented correspond clearly to a first transition into a ferroelectric phase and to a second one of strongly first order into a non-polar phase. It is interesting to note that under atmospheric pressure the first transition is sharp too and clearly of first order, but it becomes blurred under pressure up to 8 MPa, showing then a remarkable tail of polarization above T_{C1} as reproduced in figure 6(a) of [9].

2.2.3. DMAAS under hydrostatic pressure. The temperature dependences of the relative permittivity of DMAAS were measured along the ferroelectric axis at frequencies of 1, 10 and 100 kHz under various hydrostatic pressures up to 160 MPa [8]. At pressures below a critical pressure $p_C = 80$ MPa the permittivity obeys the Curie–Weiss law in the paraelectric phase. With increasing pressure the temperature T_C of the phase transition into the ferroelectric phase

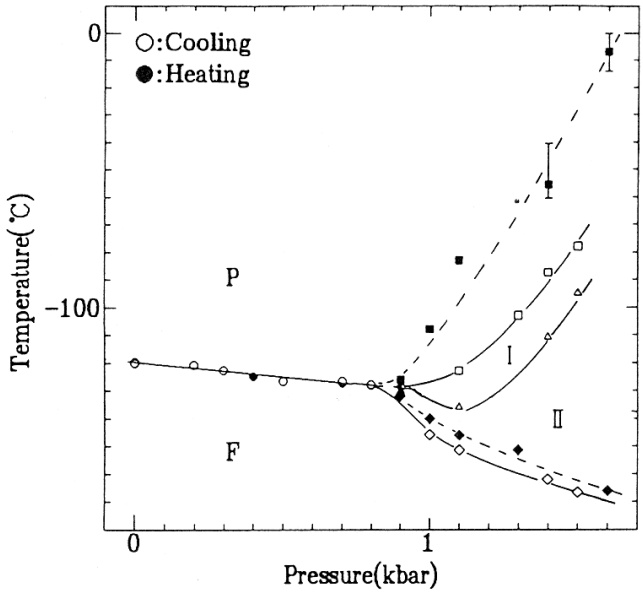

Figure 11. Pressure–temperature phase diagram of DMAAS. Open and full points indicate cooling and heating runs, respectively (from [8]).

decreases at a rate $\mathrm{d}T_C/\mathrm{d}p = -0.102$ K MPa^{-1}. There is also some decrease of the Curie–Weiss constant as well as of the maximum permittivity with pressure. On the other hand, the slope of ϵ with temperature towards T_C becomes steeper with increasing pressure in both the paraelectric and ferroelectric phases as long as the pressure is below p_C. At the critical pressure p_C itself the slope is diminished and the peak of the permittivity becomes broad. On increasing the pressure above p_C, additional temperature anomalies of ϵ appear. With cooling, ϵ shows a striking peak at T_{t1} followed by a small step-like anomaly at T_{t2} and then by a more pronounced step-like anomaly at T_{t3}. The ϵ value at T_{t1} is drastically reduced with increasing pressure whereas that at the other anomalies does not diminish so much. The temperatures T_{t1}, T_{t2} and T_{t3} of the dielectric anomalies shift remarkably with increasing pressure as shown in figure 11 and show thermal hysteresis. The authors conclude that new phases are induced under applied pressure and name them phases I and II (these must not be confused with phases I and II in DMAGaS). In these two phases the permittivity shows no dispersion, whereas pronounced dispersion has been observed in the low temperature phase. The authors assume that dispersion is caused by domain wall motion. Therefore it is concluded that the low temperature phase has ferroelectric character whereas both phases I and II are non-ferroelectric.

3. The extended DIFFOUR model

Phase transitions can be described phenomenologically by means of the Landau theory. This is true also for a transition to an incommensurate phase. For this case the Landau expansion of the free enthalpy density has to be extended by spatial gradient terms of the order parameter [23, 27]. But within Landau theory it is difficult to model a sequence of modulated phases because a number of special lock-in terms are needed. On the other hand, in order to come to an understanding of the structural reasons for the incommensurate phases, microscopic or semimicroscopic approaches are needed where the discrete nature of the system is taken into account instead of a phenomenological description.

Recently, van Raaij, van Bemmel and Janssen published a paper [11] with such a semimicroscopic approach where ground state properties and phonon dispersion curves of a classical linear chain model were studied, describing crystals with incommensurate phases of type II. The authors used the discrete frustrated ϕ^4 (DIFFOUR) model [28] extended with an extra fourth-order term. In this model the incommensurability arises if there is frustration between nearest neighbour and next nearest neighbour interactions. The potential energy of the chain is then written as

$$V = \sum_n \left\{ \frac{A}{2}x_n^2 + \frac{B}{4}x_n^4 + \frac{C}{2}(x_n - x_{n-1})^2 + \frac{D}{2}(x_n - x_{n-2})^2 + \frac{E}{2}[x_n^2(x_n - x_{n-1})^2 + x_n^2(x_n - x_{n+1})^2] \right\} \tag{2}$$

where the order parameter x_n is a component of the spontaneous polarization. In order to calculate phase diagrams, it is not necessary to vary all five parameters A, B, C, D and E; by a renormalization of the parameter set the calculation cost can be reduced. Taking $x_n' = \sqrt{B/D}x_n$ and $V' = (B/|D^2|)V$ one gets the following renormalized parameters: $A' = A/|D|$, $B' = 1$, $C' = C/|D|$, $D' = D/|D| = \pm 1$ and $E' = E/B$. The potential equation (2) can also be rewritten in the form

$$V = \sum_n \left\{ \frac{\tilde{A}}{2}x_n^2 + \frac{\tilde{B}}{4}x_n^4 + \tilde{C}x_n x_{n-1} + \tilde{D}x_n x_{n-2} + \frac{\tilde{E}}{2}\left[x_n^2(x_n - x_{n-1})^2 + x_n^2(x_n - x_{n+1})^2\right] \right\} \tag{3}$$

with $\tilde{A} = A + 2C + 2D$, $\tilde{B} = B$, $\tilde{C} = -C$, $\tilde{D} = -D$ and $\tilde{E} = E/B$, or as

$$V = \sum_n \left\{ \frac{\tilde{A}}{2}x_n^2 + \frac{\tilde{B} + \tilde{E}}{4}x_n^4 + \tilde{C}x_n x_{n-1} + \tilde{D}x_n x_{n-2} + \tilde{E}\left[x_n^2 x_{n-1}^2 - \left(x_n^2 + x_{n+1}^2\right)x_n x_{n+1}\right] \right\}. \tag{4}$$

As the model treated is one dimensional with short range interactions, there is no phase transition possible at $T \neq 0$. But if one introduces an interaction between parallel linear chains arranged in stacking planes, and one interprets the variables x_n as the averages over these planes perpendicular to the chain axes, similar expressions are obtained for such a three-dimensional system. The authors show that generally the temperature dependence is different from that of a Landau potential as not only the parameter A of the quadratic term but also the parameter C of the linear coupling term becomes temperature dependent and shows, e.g. for a paraelectric–ferroelectric transition, different slopes above and below T_C. The temperature dependences obtained are

$$A(T) = A + (3B + 4E)T, \tag{5}$$

$$C(T) = C + 6ET. \tag{6}$$

In the cited paper, phase diagrams for $T = 0$ have been calculated for the $\tilde{A}$–C and A–E parameter planes providing information about possible phase sequences. In the original DIFFOUR model with $B = 1$, $D = -1$ and $E = 0$, the $\tilde{A}$–C phase diagram is symmetric with respect to the sign change of C (see figure 4 in [11]). At low $\tilde{A}$ parameter values and with C increasing from negative to positive values, the commensurate phases becoming stable are the antiferroelectric, 1/3, 1/4, 1/5, 1/6 and ferroelectric phases with incommensurate phases in between. This result is understandable in a very simple manner. With large $|\tilde{C}|$ values the $\tilde{C}x_n x_{n-1}$ term becomes the dominating interaction and favours parallel (or antiparallel) ordering of nearest neighbours when the sign of $\tilde{C}$ is negative (or positive) because then the potential V takes a minimum. At intermediate and small $|\tilde{C}|$ values the competing nearest and next nearest neighbour interactions of the $\tilde{C}$ and $\tilde{D}$ terms lead to modulated phases. At high

$\tilde{A}$ parameter values only the paraelectric phase is stable. At ($C = 4$, $\tilde{A} = 6$) a Lifschitz point exists where the paraelectric, the ferroelectric and the incommensurate phases become equal. In the original DIFFOUR model with $E = 0$ only the parameter $\tilde{A}$ exhibits a temperature dependence. Consequently, phase sequences passed through with changing temperature are here represented by cuts of the $\tilde{A}$–C phase diagram parallel to the $\tilde{A}$ axis at a constant C parameter value. The original DIFFOUR model cannot describe our experimentally found phase sequence, because a paraelectric–ferroelectric transition needs for the model description a cut at $C > 4$ and then with lowering $\tilde{A}$ parameter, one remains only in the ferroelectric phase. That means the extended DIFFOUR model with $E \neq 0$ has to be applied. The $\tilde{A}$–C phase diagram of the extended DIFFOUR model with parameters $B = 1$, $D = -1$ and $E = 1$ presented in figure 5 of [11] shows that the $C \Longleftrightarrow -C$ symmetry disappears under the influence of the E term. Whilst the phase boundary of the paraelectric phase and also the wavelength of the phases emanating from this boundary remain unmodified under the influence of E, the phase boundaries between the commensurate and incommensurate phases are modified. They bend to lower C parameter values when the $\tilde{A}$ parameter is lowered. From the A–E phase diagram calculated with the parameters $B = 1$, $D = -1$ and $C = 1$ and presented in figure 3 of [11] one can easily see that a parameter $E < 0$ leads to a bending of the phase boundaries in the $\tilde{A}$–C phase diagram towards higher C parameter values. A phase diagram with $E < 0$ has not been calculated in [11]. Because we need it for the discussion in the next section, some numerical calculations were made, confined to the commensurate phases for mathematical simplicity but demonstrating the essentials. The phase diagram resulting from a parameter set $B = 1$, $D = -1$ and $E = -0.06$ is shown in figure 12. The stability regions of the $1/5$ and $1/3$ phases are small, so both were omitted from the phase diagram. From the results given in [11] we may conclude that the extension of the IC phases between ferroelectric and $1/4$ phases and between $1/4$ and antiferroelectric phases is also small. However, IC phases between paraelectric, ferroelectric and $1/6$ phases should be well established for $C < 4$. The phase boundary of paraelectric and IC phases calculated according to [11] is shown in figure 12 as the upper line.

Also these results can be made plausible in a simple manner. Looking at equation (4) we see that the last term $-\tilde{E}(x_n^2 + x_{n+1}^2)x_n x_{n+1}$ has a similar function for the ordering of nearest neighbours to the bilinear $\tilde{C}$ term but its influence strongly depends on the magnitude of the order parameter components x_n and x_{n+1} themselves. For small order parameter magnitudes it is negligible but for large magnitudes (at lower $\tilde{A}$ values or lower temperatures) it becomes dominant with respect to the $\tilde{C}$ term. Then, independently of the sign of $\tilde{C}$, the sign of $\tilde{E}$ alone decides the ferroelectric or antiferroelectric character of the low temperature phase. Consequently, at high $\tilde{A}$ values the magnitude and sign of $\tilde{C}$ decide the nature of the phase to which the paraphase transforms, ferroelectric, antiferroelectric, commensurate or incommensurate. At intermediate $\tilde{A}$ values the competing nearest and next nearest neighbour interactions lead to a sequence of modulated phases whereas the nature of the ground state phase at low $\tilde{A}$ is determined by the sign of $\tilde{E}$.

4. Discussion of the experimental results within the extended DIFFOUR model

Now we will show that the extended DIFFOUR model can describe the phase sequences of DMAGaS and DMAAS and their changes under applied pressure in a consistent manner. We have already shown in our former paper [10] that for negative values of the parameter $-B/16 < E < 0$, with lowering temperature the $(C(T), A(T))$ parameter curve passes through all the phases allowed within the extended DIFFOUR model when only $C(T_{\text{boundary}}) > 4$ is fulfilled at the paraelectric phase boundary. The phase sequence

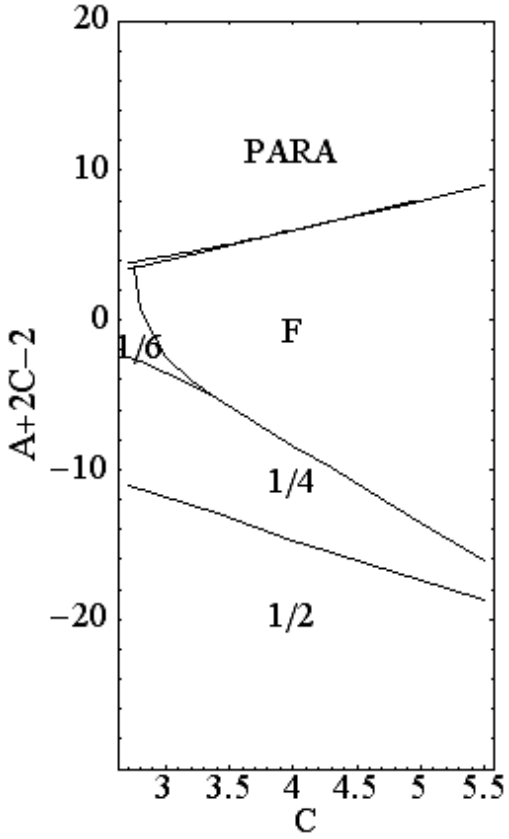

Figure 12. Phase diagram of the commensurate phases of the DIFFOUR model with $B = 1$, $D = -1$ and $E = -0.06$. Numerical calculations were made, confined to the commensurate phases for mathematical simplicity. The stability regions of the $1/5$ and $1/3$ phases are small, so both can be neglected in the phase diagram.

obtained by the model is then paraelectric–ferroelectric–IC–1/6–IC–1/5–IC–1/4–IC–1/3–IC–antiferroelectric in full correspondence with the experimentally observed sequence for DMAGaS. Even the temperature widths of the stability regions of commensurate phases are qualitatively well reproduced. A pronounced $1/4$ phase region and considerably smaller $1/6$, $1/5$ and $1/3$ phase regions have been estimated. This phase sequence is represented in the phase diagram of figure 12 by a vertical cut, e.g. at $C = 4.6$, when we ignore the temperature dependence of the parameter C because of the relatively small magnitude of E. The reason for such a parameter choice for C is that no intermediate IC phase between paraelectric and ferroelectric phases has been investigated in DMAGaS so far. One must mention, however, that with the present parameter set the $1/6$ and $1/5$ phase regions become too small with respect to the experiment.

Let us now discuss the influence of applied hydrostatic pressure on the phase diagram of DMAGaS. The most striking experimental effect is the disappearance of the ferroelectric phase at a critical pressure $p_{cr} = 8$ MPa. The basic approach to an explanation using a potential similar to equation (4) was already proposed in a former paper [29]. However, there we had misleadingly simplified the problem by assuming a simple first-order ferroelectric–antiferroelectric transition at T_{C2}. Consequently, only two sublattice polarizations were used for

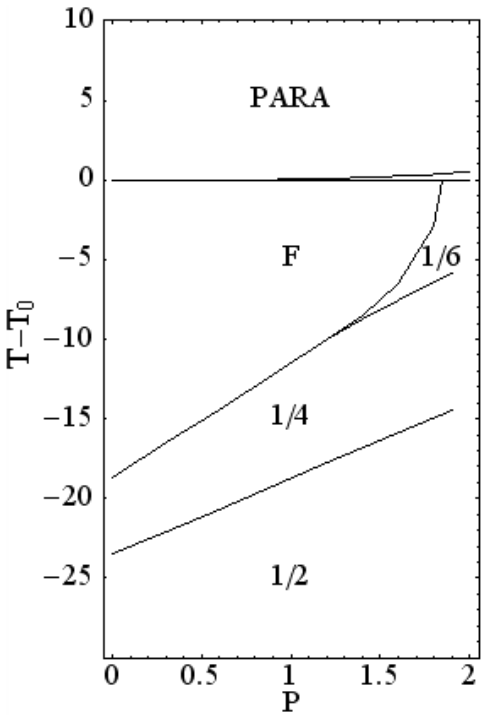

Figure 13. Pressure–temperature phase diagram of the commensurate phases calculated from the DIFFOUR model with $B = 1$, $D = -1$ and $E = -0.06$ at $C_0 = 4.6$. Note that C was taken to be pressure dependent, $C = C_0 - P$, but temperature independent. The temperature and pressure scales are in arbitrary units.

this consideration. Nevertheless, the important point is to make the parameter C of the bilinear coupling term between the sublattice polarizations pressure dependent, $C = C_0 - \Delta C_0 * P$. This becomes clear if we remember the discussion in section 3. The term $\tilde{C} x_n x_{n-1}$ stabilizes the ferroelectric phase when $-\tilde{C} = C > 0$. If C decreases under increasing pressure, the extension of the ferroelectric phase along the $\tilde{A}$ axis shrinks, and finally the ferroelectric phase is no longer stable when C is beneath a certain value as shown in figure 12. The resulting pressure–temperature diagram of the commensurate phases calculated with $C_0 = 4.6$, $\Delta C_0 = 1$ is presented in figure 13. From the diagram one sees immediately the similarity to the experimental results presented in figure 10. But within the model presented, the phase named III in figure 10 is not a homogeneous one. It corresponds for lower pressure to the $1/4$ phase and for pressures higher than what was called the critical pressure $p_{cr} = 8$ MPa to the $1/6$ phase. One should mention that the Lifschitz point must be passed with increasing pressure. Close to and above the critical pressure $p \gtrapprox p_{cr}$ the situation turns out to be more complicated. According to the model, at pressures below p_{cr} there is already no direct transition possible any longer from the paraelectric to the ferroelectric phase because of an intermediate IC phase. This could be the reason for the blurred transition at p_{cr} and the polarization tail above T_{C1} observed in the pressure experiment up to p_{cr}. At pressures approaching and above p_{cr}, with lowering temperature DMAGaS should undergo at first a paraelectric–IC transition followed then by a lock-in transition to a commensurate $1/6$ phase. With lower temperature, further transitions to the $1/4$ and antiferroelectric phases should follow, that are not yet observed experimentally.

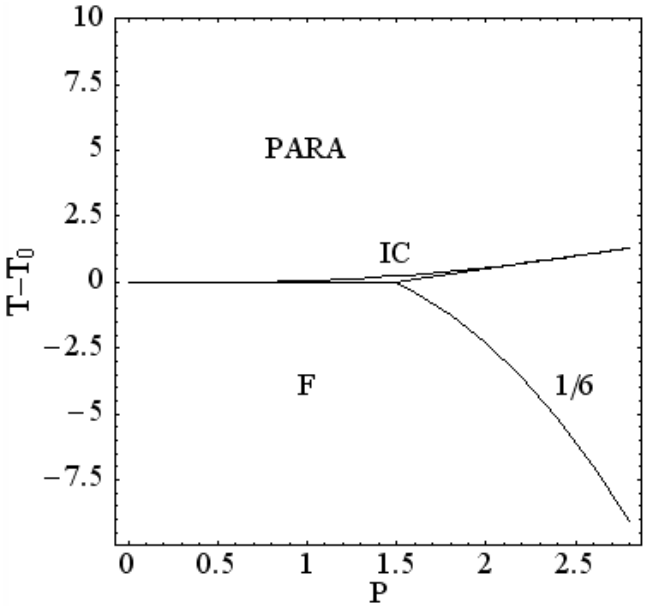

Figure 14. Pressure–temperature phase diagram of the commensurate phases calculated from the DIFFOUR model with $B = 1$, $D = -1$ and $E = +0.04$ at $C_0 = 4.6$. Note that C was taken to be pressure dependent, $C = C_0 - P$, but temperature independent. The temperature and pressure scales are in arbitrary units.

On the other hand, DMAAS shows under hydrostatic pressure higher than a critical pressure $p_C = 80$ MPa new additional anomalies of the dielectric permittivity which have been related to new phases named I and II in figure 11. For interpreting the temperature–pressure phase diagram of DMAAS in a similar manner by means of the DIFFOUR model, like in the DMAGaS case, the $\tilde{A}$–C phase diagram with $E < 0$ shown in figure 13 proves to be inapplicable. Instead we have to take advantage of the diagram calculated in [11] with $E > 0$. Using the same formalism of a pressure dependent $\tilde{C}x_n x_{n-1}$ term with $C_0 = 4.6$, $\Delta C_0 = 1$, one can consistently interpret the experimental behaviour. The result of the calculation using the DIFFOUR potential with $B = 1$, $D = -1$ and $E = +0.04$ is presented in figure 14. At atmospheric pressure, only a single transition from the paraelectric to the ferroelectric phase appears. With increasing pressure around the Lifschitz point, a new intermediate IC phase becomes stable between the paraelectric and the ferroelectric phases, which is most probably identical to phase I. The Lifschitz point may be represented in the striking broadening of the permittivity peak observed experimentally at the critical pressure p_{cr}. According to the phase diagram of figure 14, the commensurate $1/6$ phase appears with higher pressure. This new phase should correspond to the experimentally observed phase II in the pressure–temperature phase diagram shown in figure 11.

This interpretation of the pressure experiments on DMAAS and DMAGaS enables one to explain also the phase diagram of their solid solutions consistently. With an increasing content of DMAAS in the DMAAS/DMAGaS solid solution the negative parameter E must be reduced according to the content, finally change sign at some definite composition and increase further to the positive E parameter value of DMAAS. This means that for small admixtures of DMAAS in DMAGaS the size of the parameter E is reduced, leading to a less pronounced bending of the phase boundaries between the commensurate and incommensurate phases and, therefore,

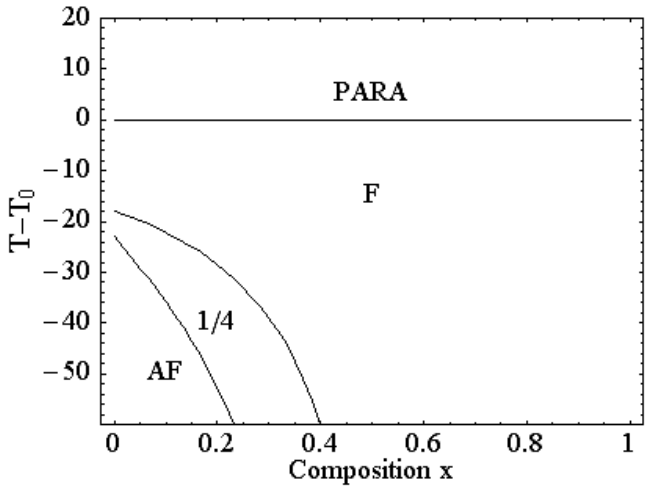

Figure 15. Composition–temperature phase diagram of the DMA$(Ga_{1-x}Al_x)$S solid solution calculated from the DIFFOUR model with $B = 1$, $D = -1$ and $C = 4.6$. A linear change of the parameter E with the composition x of the DMA$(Ga_{1-x}Al_x)$S solid solution has been assumed from $E_{Ga} = -0.06$ at $x = 0$ to $E_{Al} = +0.04$ at $x = 1$. The temperature scale has arbitrary units.

to a lower temperature T_{C2} of the transition into the commensurate $1/6$ and $1/4$ phases, as observed experimentally. Assuming a linear change of the parameter E with the composition x of the DMA$(Ga_{1-x}Al_x)$S solid solution from $E_{Ga} = -0.06$ at $x = 0$ to $E_{Al} = +0.04$ at $x = 1$, the model calculations give the phase diagram of the mixture presented in figure 15. The almost unchanged T_{C1} and the remarkably decreased T_{C2} of the $(DMAGaS)_{0.9}(DMAAS)_{0.1}$ mixed crystal studied with respect to the transition temperatures of DMAGaS are correctly interpreted. One can conclude that the replacement of Ga by Al results in a change of the next nearest neighbour interaction represented by the parameter E, whereas the nearest neighbour interaction remains nearly unchanged.

5. Conclusions

DMAAS, DMAGaS and their mixed crystals prove to be an interesting crystal family with exceptional commensurate/incommensurate phase sequences. The phase sequence in DMAGaS, with a paraelectric–ferroelectric transition at high temperatures, followed by incommensurate and commensurate phases at medium temperatures and an antiferroelectric lock-in phase at low temperatures, is quite singular and to our knowledge not yet observed in any other crystal. The various phase transition temperatures of DMAGaS are shifted under the influence of hydrostatic pressure and DMAAS admixture. In DMAAS, new phases have been induced under hydrostatic pressure. All these complex experimental findings can be qualitatively understood within the semimicroscopic extended DIFFOUR model in a very consistent manner. Qualitatively, the extended DIFFOUR model provides phase diagrams which give a consistent description of the phase sequences observed experimentally as well as their variation with pressure and composition. The chain-like structure upon which the model is based is given in the crystal in the form of the $–DMA_{(i)}–Ga/Al(H_2O)_{6(i)}–DMA_{(i+1)}–Ga/Al(H_2O)_{6(i+1)}–$ chains where the DMA molecules represent the orientable electric dipoles. The model considerations uncover that the $Ga/Al(H_2O)_6$ octahedra act as mediators for the interaction between the DMA dipoles. In order to complete the model description of this

outstanding crystal family, further experimental studies of the DMAAS/DMAGaS mixed crystals should be carried out and quantitative calculations of the phase diagram within the DIFFOUR model should be performed.

Acknowledgment

The work was supported by grant BO 1080/7-2 of the Deutsche Forschungsgemeinschaft.

References

[1] Andreev E F, Varikash V M and Shuvalov A L 1991 *Izv. AN SSSR, Ser. Fiz.* **55** 572
[2] Sobiestianskas R, Grigas J, Andreev E F and Varikash V M 1992 *Phase Transit.* **40** 85
[3] Pietraszko A, Lukaszewicz K and Kirpichnikova L F 1993 *Pol. J. Chem.* **67** 1877
[4] Pietraszko A, Lukaszewicz K and Kirpichnikova L F 1995 *Pol. J. Chem.* **69** 920
[5] Dacko S and Czapla Z 1996 *Ferroelectrics* **189** 143
[6] Czapla Z and Rykacz H 1997 *Ferroelectr. Lett.* **22** 121
[7] Tchukvinskyi R, Cach R and Czapla Z 1998 *Z. Naturf.* a **53** 105
[8] Yasuda N, Tajima H and Czapla Z 1994 *Phys. Lett.* A **192** 137
[9] Yasuda N, Kaneda A and Czapla Z 1999 *Ferroelectrics* **223** 71
[10] Völkel G, Böttcher R, Michel D and Czapla Z 2003 *Phys. Rev.* B **67** 024111
[11] van Raaij G H F, van Bemmel K J H and Janssen T 2000 *Phys. Rev.* B **62** 3751
[12] Dolinšek J, Klanjšek M, Arčon D, Kim H J, Seliger J and Žagar V 1999 *Phys. Rev.* B **59** 3460
[13] Völkel G, Alsabbagh N, Böttcher R, Michel D, Milsch B, Czapla Z and Furtak J 2000 *J. Phys.: Condens. Matter* **12** 4553
[14] Stasyuk I V, Velychko O V, Czapla Z and Czukwinski R 2000 *Cond. Matter Phys.* **3** 213
[15] Stasyuk I V and Velychko O V 2001 *Phase Transit.* **73** 483
[16] Alsabbagh N, Michel D, Furtak J and Czapla Z 1998 *Phys. Status Solidi* a **167** 77
[17] Bednarski W, Waplak S and Kirpichnikowa L F 1999 *J. Phys.: Condens. Matter* **11** 1567
[18] Bednarski W, Waplak S and Kirpichnikowa L F 1999 *J. Phys. Chem. Solids* **60** 1669
[19] Völkel G, Alsabbagh N, Böttcher R, Michel D and Czapla Z 1999 *Phys. Status Solidi* b **215** R5
[20] Völkel G, Böttcher R, Michel D and Czapla Z 2001 *Phys. Status Solidi* b **223** R6
[21] Völkel G, Böttcher R, Michel D and Czapla Z 2002 *Ferroelectrics* **268** 181
[22] Völkel G, Alsabbagh N, Banys J, Bauch H, Böttcher R, Gutjahr M, Michel D and Pöppl A 2002 *Adv. Solid State Phys.* **42** 241
[23] Blinc R and Levanyuk A P (ed) 1986 *Incommensurate Phases in Dielectrics* (Amsterdam: North-Holland)
[24] Gemperle C, Schweiger A and Ernst R 1991 *Chem. Phys. Lett.* **178** 565
[25] Banys J, Völkel G, Böttcher R, Michel D and Czapla Z 2005 *Phase Transit.* **78** 337
[26] Sobiestianskas R, Grigas J, Andreev E F and Varikash V M 1992 *Phase Transit.* **40** 85
[27] Strukov B A and Levanyuk A P 1998 *Ferroelectric Phenomena in Crystals* (Berlin: Springer)
[28] Janssen T 1986 *Incommensurate Phases in Dielectrics* vol 1, ed R Blinc and A P Levanyuk (Amsterdam: North-Holland) p 67
[29] Völkel G 2000 *Phys. Status Solidi* b **217** R3